CONEM 2016
CONGRESSO NACIONAL DE ENGENHARIA MECÂNICA
21 - 25 AGOSTO DE 2016
FORTALEZA - CEARÁ

POSITION, VELOCITY AND HEADING ESTIMATION FOR UNMANNED AERIAL VEHICLES USING CAMERA AND INERTIAL SENSORS

Author1, e-mail[1]
Author2, e-mail[1]
Author3, e-mail[2]

[1]Institution's name, Address
[2]Institution's name, Address

Abstract code: CON-2016-0515

Abstract: *Precise and robust navigation of Unmanned Aerial Vehicles (UAV) in GNSS-denied environments is a relevant research topic, especially for autonomous systems. Most of the proposed solutions to this problem rely on expensive and high-precision equipment, thus limiting the accessibility of this technology for research. This work proposes a position, velocity and heading estimation algorithm for multirotor UAV using low-cost components, such as a gyro-stabilized platform containing a downward-facing onboard camera, inertial sensors and an ultrasonic range sensor, using a two-axis gimbal. The estimation algorithm is composed of three steps. At first, the vehicle must detect and identify visible landmarks by processing the images. Second, the algorithm computes the vectors from the camera center to each of the visible landmarks. Finally, measurements from the inertial sensors, ultrasonic range sensor and the landmark's vector measurements are fused with an Extended Kalman Filter (EKF) to estimate the vehicle's position, velocity and heading as well as accelerometer and rate-gyro biases. A map of landmarks is assumed available and the vehicle is supposed to operate indoors. The method is evaluated via extensive Monte Carlo simulations, which show its effectiveness and some of its properties.*
Keywords: *Extended Kalman filter, Visual-inertial navigation, Sensor fusion, Unmanned Aerial Vehicle.*

1 INTRODUCTION

Unmanned Aerial Vehicles (UAV) have attracted great attention in recent years due to its wide range of possible applications in both military and civil areas. Special attention is given to autonomous UAV, which represents a multidisciplinary challenge. Autonomous vehicles relies on a precise state estimation system, which, in turn, relies on the Hardware used, such as the onboard sensors and digital processing unit, responsible for the sensor fusion algorithm. The development of autonomous UAV represents a significant step in technology and some of recent application examples include terrain mapping for precision agriculture (Primicerio *et al.*, 2012), border surveillance (Beard *et al.*, 2006), building surveillance (Hoffmann *et al.*, 2008), and search and rescue (Erdos *et al.*, 2013).

Navigation research was mostly focused on vehicles operating in outdoor environments, where the state estimation problem was extensively tackled using GPS/INS systems (Erdos *et al.*, 2013; Wendel *et al.*, 2006). Recently, the attention has become to precise and robust state estimation in GNSS-denied environment, such as indoor environments (Gini and Marchi, 2002; Thrun, 2002). As examples of recent works, in Gini and Marchi (2002), the author uses a single camera on top of a mobile robot to track its position based on tracked objects on the floor. In Trawny *et al.* (2007), the authors fuse measurements from high-end gimbaled inertial sensors with a camera and using an EKF to estimate the position and velocity of an aircraft during entry, descent and landing on celestial bodies with validation on real data. The authors rely on mapped landmarks, such as craters or other visual features. Moreover, in García Carrillo *et al.* (2012) great work was done using stereo visual odometry and inertial measurements fused by a Kalman Filter (KF), in order to a multirotor vehicle autonomously navigate through an indoor environment. Nonetheless, none of the aforementioned works are concerned with the accessibility of this technology for research, as the sensors used are usually expensive and accurate.

The sensor fusion algorithm used in the state estimation problem is a well-known problem and represents an active field of study. One of the most popular methods for this purpose is the Kalman Filter, first introduced in Kalman (1960). The method belongs to the class of *minimum mean square error* (MMSE) estimators and is a particular case of the optimal

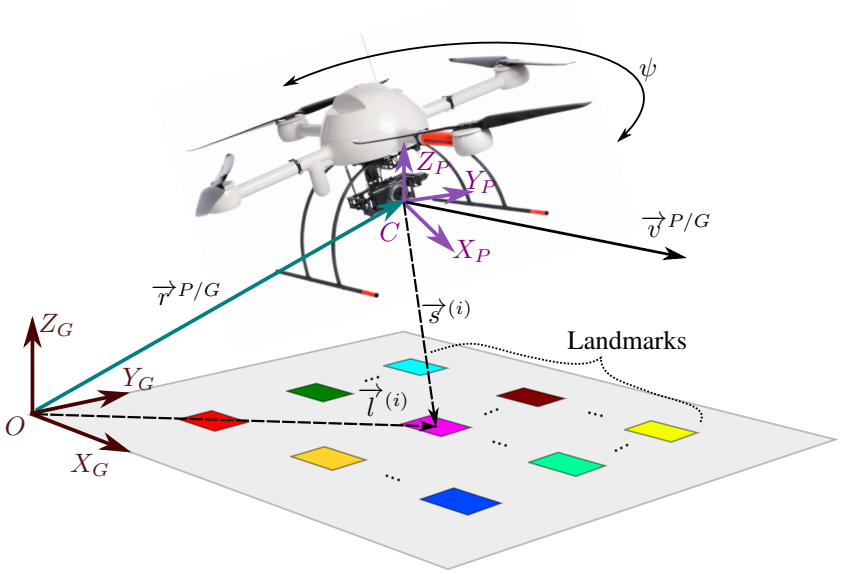

Figure 1: The navigation platform and the Cartesian Coordinate Systems (CCS).

Bayesian Filter (Arulampalam *et al.*, 2001) for linear and normally distributed variables. For nonlinear problems, several adaptations to the original Kalman Filter are made in order to overcome the nonlinearities, such as the Unscented Kalman Filter (UKF) (Zhang *et al.*, 2015), Ensemble Kalman Filter (EnKF) (Evensen, 2003) and the Extended Kalman Filter (EKF) (Gelb, 1974).

In the present paper, the proposed estimation problem focuses in navigation of an UAV for indoor environments using a downward-facing camera, inertial sensors and an ultrasonic range finder, using an Extended Kalman Filter algorithm for sensor fusion. The sensors are fixed in a gyro-stabilized platform with two degrees-of-freedom (DOF), in which enables the platform to remain parallel to the ground plane. The vehicle navigates through an environment with known visible landmarks, that are captured by the camera, thus providing a position, velocity and heading estimation of the UAV's platform. This estimation is fused with the inertial sensors measurements in an Extended Kalman Filter algorithm, thereby obtaining a preciser estimate of the desired states, as well as accelerometer and rate-gyro biases. In Section 2, the problem structure is comprehensively devised with its proposed hypothesis, dynamics and considerations. Section 3 presents a solution for the indicated problem and devise the used EKF algorithm. Section 4 presents the evaluation of the system through an extensive Monte Carlo simulation, where it gives considerations regarding the relationship between the precision of the estimator and the number of landmarks used. Finally, Section 5 presents the final conclusions.

2 PROBLEM DEFINITION

This section defines a vision-inertial navigation problem suitable for UAVs. To begin with, Section 2.1 presents the kinematics equations. Section 2.2 specifies the measurement equations. Finally, Section 3.1 provides a camera model for determining a three-dimensional point from a two-dimentional image and an ultrassonic range finder.

2.1 Dynamic Model

Figure 1 illustrates the navigation platform as the two Cartesian coordinate systems (CCS) for describing the problem. $S_{\mathrm{G}} = \{X_{\mathrm{G}}, Y_{\mathrm{G}}, Z_{\mathrm{G}}\}$ is fixed to the ground at the point O. $S_{\mathrm{P}} = \{X_{\mathrm{P}}, Y_{\mathrm{P}}, Z_{\mathrm{P}}\}$ represents the platform CCS and is centered at C.

The platform consists of a gyro-stabilized two-axis gimbal, which is parallel to the local horizontal. It holds a triaxial accelerometer aligned with S_{P}, a single-axis rate-gyro as well as an ultrassonic range sensor aligned with Z_{P}, and a downward pointing camera with the optical axis aligned with the negative Z_{P} axis.

The present work aims at providing a precise and robust solution to the position $\overrightarrow{r}^{P/G}$, velocity $\overrightarrow{r}^{P/G}$ and heading angle ψ of an UAV. The sensors chosen for this purpose consists of a triaxial accelerometer aligned with the S_{P} axes, a rate-gyro aligned with the Z_{P} axis, a downward pointing camera and an ultrasonic range finder.

Having defined the prior hypotheses, let the us now consider the S_{G} representation of $\overrightarrow{r}^{P/G}$ and $\overrightarrow{v}^{P/G}$ denoted, respectively, by $\mathbf{r}_G^{P/G}$ and $\mathbf{v}_G^{P/G}$. The non-linear set of equations that describes the dynamic $\mathbf{r}_G^{P/G}$ and $\mathbf{v}_G^{P/G}$ are denoted as follows:

$$\dot{\mathbf{r}}_G^{P/G} = \mathbf{v}_G^{P/G} + {}^{r}\mathbf{w} \tag{1}$$

$$\dot{\mathbf{v}}_G^{P/G} = \left[\mathbf{D}^{P/G}(\psi)\right]^{\mathrm{T}}(\breve{\mathbf{a}}_P - \boldsymbol{\beta}_a) + \mathbf{g}_G + {}^{v}\mathbf{w} \tag{2}$$

$$\dot{\psi} = \breve{\omega}_z - \beta_g + {}^{\psi}\mathbf{w} \tag{3}$$

$$\dot{\beta}_g = {}^{g}w \tag{4}$$

$$\dot{\boldsymbol{\beta}}_a = {}^{a}\mathbf{w} \tag{5}$$

where ${}^{j}\mathbf{w}$ is defined as the noise of the state j, with j representing each unique state in the vector-state; $\breve{\mathbf{a}}$ and $\breve{\omega}_z$ denotes the measurements taken from the accelerometer and the gyrometer, respectively. Likewise, $\boldsymbol{\beta}_a$ and β_g represents the bias of the respective measurements. Also,

$$\boldsymbol{g}_G \triangleq \begin{bmatrix} 0 & 0 & -g \end{bmatrix}^{\mathrm{T}}, \tag{6}$$

$$\mathbf{D}^{P/G} = \begin{bmatrix} C\psi & S\psi & 0 \\ -S\psi & C\psi & 0 \\ 0 & 0 & 1 \end{bmatrix} \tag{7}$$

where $\mathbf{D}^{P/G}(\psi)$ is defined as the rotation matrix of the frame S_{G} to the frame S_{P} around the Z_{P} axis (Shuster, 1993) and, for brevity, $C\psi$ and $S\psi$ represents the $cos(\psi)$ and $sin(\psi)$, respectively. The vector $\boldsymbol{g}_g$ is the gravity acceleration vector in respect to S_{G}.

Now, Eq. (1)-(5) can be rewritten in the continuous state-space form

$$\dot{\boldsymbol{x}}(t) = \boldsymbol{f}(\boldsymbol{x}(t), \boldsymbol{u}(t)) + \boldsymbol{w}(t) \tag{8}$$

where

$$\boldsymbol{f}(\boldsymbol{x}(t), \boldsymbol{u}(t)) = \begin{bmatrix} v_{G,x}^{P/G} \\ v_{G,y}^{P/G} \\ v_{G,z}^{P/G} \\ C\psi(\breve{a}_{P,x} - \beta_{a,x}) - S\psi(\breve{a}_{P,y} - \beta_{a,y}) \\ S\psi(\breve{a}_{P,x} - \beta_{a,x}) + C\psi(\breve{a}_{P,y} - \beta_{a,y}) \\ \breve{a}_{P,z} - \beta_{a,z} - g \\ \breve{w}_z - \beta_g \\ \mathbf{0}_{4\times 1} \end{bmatrix} \tag{9}$$

with state-vector defined as

$$\mathbf{x}(t) \triangleq \begin{bmatrix} \left(\boldsymbol{r}_G^{G/P}\right)^{\mathrm{T}} & \left(\boldsymbol{v}_G^{G/P}\right)^{\mathrm{T}} & \psi & \beta_g & (\boldsymbol{\beta}_a)^{\mathrm{T}} \end{bmatrix}^{\mathrm{T}} \in \mathbb{R}^{11}, \tag{10}$$

known input vector

$$\mathbf{u}(t) \triangleq \begin{bmatrix} (\breve{\boldsymbol{a}}_P)^{\mathrm{T}} & \breve{\omega}_z \end{bmatrix}^{\mathrm{T}} \in \mathbb{R}^4 \tag{11}$$

and a state noise vector

$$\mathbf{w}(t) \triangleq \begin{bmatrix} ({}^{r}\mathbf{w})^{\mathrm{T}} & ({}^{v}\mathbf{w})^{\mathrm{T}} & {}^{\psi}w & {}^{g}w & ({}^{a}\mathbf{w})^{\mathrm{T}} \end{bmatrix}^{\mathrm{T}} \in \mathbb{R}^{11} \tag{12}$$

where the noise is considered a zero-mean Gaussian white-noise with covariance matrix denoted by $\boldsymbol{Q}(t)$.

2.2 Measurement Equation

The Figure 2 shows the navigation system with a pin-hole camera model (Ponce and Forsyth, 2012; Hartley and Zisserman, 2015) and a map of landmarks. It is introduced a new CCS, the camera Cartesian Coordinate System denoted by $S_{\mathrm{C}} = \{X_{\mathrm{C}}, Y_{\mathrm{C}}, Z_{\mathrm{C}}\}$ with origin also coincident with C. Therefore, $\overrightarrow{r}^{P/G} = \overrightarrow{r}^{C/G}$.

Each landmark is represented in S_{G} as a position vector $\overrightarrow{l}^{(i)}$, for $i = 1, ..., n$; where n is the total number of known landmarks in the environment. In this work it is assumed that a prior map of landmarks is previously given. Similarly, the landmarks can be represented in S_{C} and is denoted by $\overrightarrow{s}^{(i)}$, for $i = 1, ..., n$. Hence, from Figure 2 one could geometrically obtain $\overrightarrow{r}^{C/G}$ for the i-th landmark as

$$\overrightarrow{r}^{C/G} = \overrightarrow{s}^{(i)} - \overrightarrow{l}^{(i)} \tag{13}$$

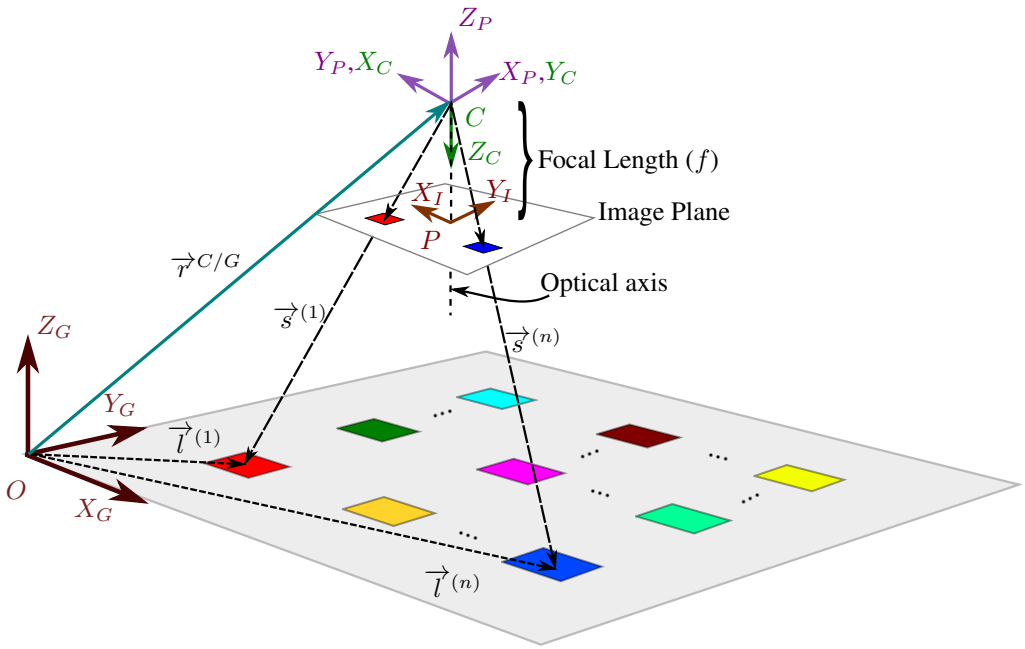

Figure 2: Illustration of the navigation environment and a pinhole camera model.

Representing the Eq. (13) in S_{G}, we obtain

$$\mathbf{r}_G^{C/G} = \mathbf{l}_G^{(i)} - \left[\boldsymbol{D}^{C/P}\boldsymbol{D}^{P/G}\left(\psi\right)\right]^{\mathrm{T}} \boldsymbol{s}_C^{(i)} \tag{14}$$

Hence

$$\boldsymbol{s}_C^{(i)} = \boldsymbol{D}^{C/P}\boldsymbol{D}^{P/G}\left(\psi\right)\left(\mathbf{l}_G^{(i)} - \mathbf{r}_G^{C/G}\right) \tag{15}$$

where the rotation matrix $\boldsymbol{D}^{C/P}$ is obtained from the rotation of the frame S_{P} to frame S_{C}; and $\boldsymbol{D}^{P/G}$ consists of a rotation by ψ around the Z_{C} axis. From Fig. 2, $\boldsymbol{D}^{C/P}$ is obtained by rotating by $-90°$ around the Z_{P} axis followed by a rotation of $180°$ around the new $Y_{\mathrm{P}} = Y_{\mathrm{C}}$ axis. The final rotation matrix is defined as follows

$$\boldsymbol{D}^{C/P} = \begin{bmatrix} 0 & 1 & 0 \\ 1 & 0 & 0 \\ 0 & 0 & -1 \end{bmatrix} \tag{16}$$

thus

$$\boldsymbol{D}^{C/G} = \begin{bmatrix} -\sin\psi & \cos\psi & 0 \\ \cos\psi & \sin\psi & 0 \\ 0 & 0 & -1 \end{bmatrix} \tag{17}$$

Therefore, using the definition of Eq. (7) and replacing by its measurements at time $t_k = kT$, with T representing the measurement sampling interval, it is possible to obtain

$$\check{\boldsymbol{s}}_{C_k}^{(i)} = \begin{bmatrix} -\sin\psi_k & \cos\psi_k & 0 \\ \cos\psi_k & \sin\psi_k & 0 \\ 0 & 0 & -1 \end{bmatrix}\left(\mathbf{l}_{G_k}^{(i)} - \mathbf{r}_{G_k}^{C/G}\right) + \boldsymbol{v}_k^{(i)} \tag{18}$$

where $\left\{\boldsymbol{v}_k^{(i)}\right\} \in \mathbb{R}^3$ is a zero-mean Gaussian white sequence, considered i.i.d., with covariance matrix $\boldsymbol{R}_{\boldsymbol{k}}^{(i)}$. Furthermore, the Eq. (18) is rewritten in a general form

$$\boldsymbol{y}_k^{(i)} = \boldsymbol{h}^{(i)}\left(\boldsymbol{x}_k\right) + \boldsymbol{v}_k^{(i)} \tag{19}$$

where $\boldsymbol{x}$ is the state vector defined in Eq. (10), $\boldsymbol{v}_k^{(i)} \in \mathbb{R}^3$ is the measurement noise vector corresponding to the i-th landmark. From Eq. (18) and Eq. (19), we obtain

$$\boldsymbol{y}_k^{(i)} \triangleq \boldsymbol{s}_{C_k}^{(i)} \tag{20}$$

and

$$\boldsymbol{h}^{(i)}\left(\boldsymbol{x}_k\right) \triangleq \begin{bmatrix} -S\psi\left(l_x^{(i)} - r_{G,x}^{C/G}\right) + C\psi\left(l_y^{(i)} - r_{G,y}^{C/G}\right) \\ C\psi\left(l_x^{(i)} - r_{G,x}^{C/G}\right) + S\psi\left(l_y^{(i)} - r_{G,y}^{C/G}\right) \\ -l_z^{(i)} + r_{G,z}^{C/G} \end{bmatrix} \tag{21}$$

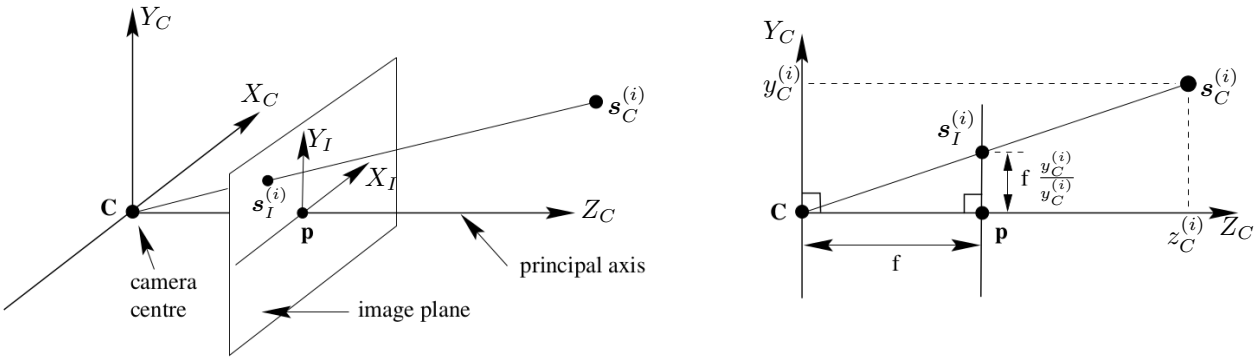

Figure 3: Pinhole camera geometry adapted from Hartley and Zisserman (2015).

Equation (21) represents the non-linear measurement equation defined to an arbitrary i-th landmark. It is important to realize that the full measurement equation has a different size depending on the number of visible landmarks measured by the camera at a given sample time. Therefore, if at a given sample time t_k, we have q measured landmarks, the full measurement equation can be obtained as

$$\boldsymbol{y}_k = \boldsymbol{h}\left(\boldsymbol{x}_k\right) + \boldsymbol{v}_k, \tag{22}$$

where $\boldsymbol{y}_k \triangleq \begin{bmatrix} \boldsymbol{y}_k^{(1)} & \boldsymbol{y}_k^{(2)} & \dots & \boldsymbol{y}_k^{(q)} \end{bmatrix}^{\mathrm{T}}$, $\boldsymbol{v}_k \triangleq \begin{bmatrix} \boldsymbol{v}_k^{(1)} & \boldsymbol{v}_k^{(2)} & \dots & \boldsymbol{v}_k^{(q)} \end{bmatrix}^{\mathrm{T}}$ and

$$h\left(\boldsymbol{x}_k\right) \triangleq \begin{bmatrix} \boldsymbol{h}^{(1)}\left(\boldsymbol{x}_k\right) \\ \boldsymbol{h}^{(2)}\left(\boldsymbol{x}_k\right) \\ \vdots \\ \boldsymbol{h}^{(q)}\left(\boldsymbol{x}_k\right) \end{bmatrix} \tag{23}$$

3 PROBLEM SOLUTION

In the previous section the estimation problem was devised using inertial sensors. Section 3.1 depicts the camera model used in order to obtain an estimate of the vehicle's states. Section 3.2 presents a review of a first-order Extended Kalman Filter estimator, which was chosen to solve the proposed estimation problem. Finally, the section proposes an estimation algorithm at the end, as well as implementation considerations.

3.1 Camera Model and Range Sensor

As stated early in Section 2, the measurement equation relies on the correct retrieval of the vector $\boldsymbol{s}_C^{(i)}$, for $i = 1, ..., q$, from camera measurements. In order to achieve this goal, a camera model must be devised to describe the projection of the points in the space onto an image plane. According to Hartley and Zisserman (2015) and Ponce and Forsyth (2012), a simple camera model can be defined as in Figure 3.

Primarily, it is necessary to define an image coordinate system $S_{\mathrm{I}} = \{X_{\mathrm{I}}, Y_{\mathrm{I}}\}$, with origin at point P, denoted as the principal point (Ponce and Forsyth, 2012), which represents the exact point where the Z_{C} axis, also known as the principal axis (Hartley and Zisserman, 2015), intercepts the image plane; and the X_{I} and Y_{I} axes are parallel with X_{I} and Y_{I} axes, respectively. From Fig. 3 and Fig. 2 it is possible to describe a projection model of the i-th landmark $\boldsymbol{s}_C^{(i)}$, represented in the S_{C} reference frame, onto the image plane, defined here as $\boldsymbol{s}_I^{(i)}$. From trigonometry we obtain (Ponce and Forsyth, 2012)

$$x_{I_k}^{(i)} = \frac{f}{z_{C_k}^{(i)}} x_{C_k}^{(i)}, \qquad y_{I_k}^{(i)} = \frac{f}{z_{C_k}^{(i)}} y_{C_k}^{(i)}, \tag{24}$$

where $x_{C_k}^{(i)}$, $y_{C_k}^{(i)}$ and $z_{C_k}^{(i)}$ are the components of $\boldsymbol{s}_C^{(i)}$ and f is the camera's focal length at time t_k. Likewise, $x_{I_k}^{(i)}$ and $y_{I_k}^{(i)}$ are the components of the projection of $\boldsymbol{s}_C^{(i)}$ onto the image plane denoted by S_{I}.

Thus inverting Eq. (24) and replacing the true variables $x_{C_k}^{(i)}$, $y_{C_k}^{(i)}$ and $z_{C_k}^{(i)}$ by the corresponding measurements, we obtain

$$\check{x}_{C_k}^{(i)} = \frac{\check{z}_{C_k}^{(i)}}{f} \check{x}_{I_k}^{(i)} \qquad \check{y}_{C_k}^{(i)} = \frac{\check{z}_{C_k}^{(i)}}{f} \check{y}_{I_k}^{(i)}, \tag{25}$$

where $\check{z}_{C_k}^{(i)}$ is obtained directly from an ultrasonic range finder, that is aligned with the Z_{C} axis.

It is important to realize that, in practice, in order to obtain the vector $\check{\boldsymbol{s}}_{I_k}^{(i)}$, it is necessary to acquire, process and manipulate the image to find the desired landmarks, which is not in the scope of this work. In Section 4 we present a test environment using Simulink 3D Animation (MathWorks, 2016) and we adopt that the landmarks are simplified and its location are easily obtained without the usage of complex image processing algorithms. In practice, the algorithms developed in the subsequent sections depends on a reliable landmark position estimation through image processing, which can be found in great detail in Bay *et al.* (2006) and Lowe (1999).

3.2 Extended Kalman Filter

Consider the dynamic's state-space given by Eq. (8) in discrete time

$$\boldsymbol{x}_{k+1} = \boldsymbol{f}\left(\boldsymbol{x}_k, \boldsymbol{u}_k\right) + \boldsymbol{w}_k \tag{26}$$

and its measurement equation given by Eq. (22)

$$\boldsymbol{y}_{k+1} = \boldsymbol{h}\left(\boldsymbol{x}_k\right) + \boldsymbol{v}_{k+1} \tag{27}$$

where $\{\boldsymbol{w}_k\} \in \mathbb{R}^{11}$ and $\{\boldsymbol{v}_{k+1}\} \in \mathbb{R}^{3q}$ are assumed additive uncorrelated zero-mean Gaussian white-noises with covariance matrices $\boldsymbol{Q}_k$ and $\boldsymbol{R}_{k+1}$, respectively.

The main objective of the Extended Kalman Filter is to obtain an estimate $\hat{\boldsymbol{x}}_{k|k}$ of the system state $\boldsymbol{x}_k$ that minimizes the following cost function

$$J_k \triangleq \mathbb{E}\left[\left(\boldsymbol{x}_k - \hat{\boldsymbol{x}}_{k|k}\right)^{\mathrm{T}}\left(\boldsymbol{x}_k - \hat{\boldsymbol{x}}_{k|k}\right)\right], \forall k \tag{28}$$

where $\mathbb{E}$ denotes the expectation operator and $\hat{\boldsymbol{x}}_{k|k} \triangleq \mathbb{E}\left[\boldsymbol{x}_k|\boldsymbol{y_k}\right] \in \mathbb{R}^{11}$, for $\mathbb{E}\left[a|b\right]$ representing the expectation of a given the information of b. Furthermore, the state error covariance matrix is obtained by $\boldsymbol{P}_k \triangleq \mathbb{E}\left[\left(\boldsymbol{x}_k - \hat{\boldsymbol{x}}_{k|k}\right)\left(\boldsymbol{x}_k - \hat{\boldsymbol{x}}_{k|k}\right)^{\mathrm{T}}\right] \in \mathbb{R}^{11\times 11}$. The initial condition $\boldsymbol{x}_0$ is also assumed a Gaussian random variable with mean and correlation matrix defined by $\overline{\boldsymbol{x}}$ and $\overline{\boldsymbol{P}}$, respectively; and uncorrelated to $\boldsymbol{w}_k$ and $\boldsymbol{v}_k$.

The Extended Kalman Filter consists of two main steps. The first step is defined as the propagation step and the goal is to find a predicted state estimate $\hat{\boldsymbol{x}}_{k+1|k} \triangleq \mathbb{E}\left[\boldsymbol{x}_{k+1}|\boldsymbol{y_k}\right]$, as well as its predicted state error covariance matrix $\boldsymbol{P}_{k+1} \triangleq \mathbb{E}\left[\left(\boldsymbol{x}_{k+1} - \hat{\boldsymbol{x}}_{k+1|k}\right)\left(\boldsymbol{x}_{k+1} - \hat{\boldsymbol{x}}_{k+1|k}\right)^{\mathrm{T}}\right]$, and a predicted measurement estimate $\hat{\boldsymbol{y}}_{k+1|k} \triangleq \mathbb{E}\left[\boldsymbol{y}_{k+1}|\boldsymbol{y_k}\right]$ using the dynamic and measurement equations. Assuming that the functions given by Eq. (26)-(27) are sufficiently smooth, the nonlinear functions $\boldsymbol{f}\left(\boldsymbol{x}_k, \boldsymbol{u}_k\right)$ and $\boldsymbol{h}\left(\boldsymbol{x}_k\right)$ can be linearized by expanding a first-order Taylor series about the estimate $\hat{\boldsymbol{x}}_{k|k}$ (Anderson *et al.*, 1982)

$$\boldsymbol{f}\left(\boldsymbol{x}_{k|k}, \boldsymbol{u}_k\right) \approx \boldsymbol{f}\left(\hat{\boldsymbol{x}}_{k|k}, \boldsymbol{u}_k\right) + \boldsymbol{F}_k\left(\boldsymbol{x}_k - \hat{\boldsymbol{x}}_{k|k}\right) \tag{29}$$

$$\boldsymbol{h}\left(\boldsymbol{x}_{k|k}\right) \approx \boldsymbol{f}\left(\hat{\boldsymbol{x}}_{k|k}\right) + \boldsymbol{H}_{k+1}\left(\boldsymbol{x}_k - \hat{\boldsymbol{x}}_{k|k}\right) \tag{30}$$

where

$$\boldsymbol{F}_k \triangleq \left[\frac{\partial}{\partial \boldsymbol{x}}\boldsymbol{f}\left(\boldsymbol{x}, \boldsymbol{u}_k\right)\right]_{\boldsymbol{x}=\hat{\boldsymbol{x}}_{k|k}} \qquad \boldsymbol{H}_{k+1} \triangleq \left[\frac{\partial}{\partial \boldsymbol{x}}\boldsymbol{h}\left(\boldsymbol{x}\right)\right]_{\boldsymbol{x}=\hat{\boldsymbol{x}}_{k+1|k}} \tag{31}$$

are the Jacobian matrices of $\boldsymbol{f}\left(\boldsymbol{x}_{k|k}, \boldsymbol{u}_k\right)$ and $\boldsymbol{h}\left(\boldsymbol{x}_{k|k}\right)$, respectively. Therefore, it is possible to obtain the predicted estimate using a structure similar to the linear Kalman Filter (Gelb, 1974) as follows:

$$\hat{\boldsymbol{x}}_{k+1|k} \approx \boldsymbol{f}\left(\hat{\boldsymbol{x}}_{k|k}, \boldsymbol{u}_k\right) \tag{32}$$

$$\hat{\boldsymbol{y}}_{k+1|k} \approx \boldsymbol{h}\left(\hat{\boldsymbol{x}}_{k|k}\right) \tag{33}$$

Furthermore, the predicted state covariance matrix, also called the residual covariance, is obtained by the so-called discrete-time Riccati equation (Anderson *et al.*, 1982)

$$\boldsymbol{P}_{k+1|k} = \boldsymbol{F}_k\boldsymbol{P}_{k|k}\boldsymbol{F}_k^{\mathrm{T}} + \boldsymbol{Q}_k \tag{34}$$

The second step of the EKF is defined as the update step. This step uses the measurement y_{k+1} at time t_{k+1} to update the predicted state estimate $\hat{\boldsymbol{x}}_{k+1|k}$ and state covariance $\boldsymbol{P}_{k+1|k}$, thereby obtaining the desired estimates $\hat{\boldsymbol{x}}_{k+1|k+1}$ and $\boldsymbol{P}_{k+1|k+1}$ with

$$\hat{\boldsymbol{x}}_{k+1|k+1} = \hat{\boldsymbol{x}}_{k+1|k} + \boldsymbol{K}_{k+1}\left(\boldsymbol{y}_{k+1} - \hat{\boldsymbol{y}}_{k+1|k}\right) \tag{35}$$

$$\boldsymbol{P}_{k+1|k+1} = \boldsymbol{P}_{k+1|k} - \boldsymbol{K}_{k+1}\boldsymbol{H}_{k+1}\boldsymbol{P}_{k+1|k}, \tag{36}$$

where $\boldsymbol{K}_{k+1}$ is referred as the Kalman gain matrix, which is given by

$$\boldsymbol{K}_{k+1} = \boldsymbol{P}_{k+1|k}\boldsymbol{H}_{k+1}^{\mathrm{T}}\left(\boldsymbol{H}_{k+1}\boldsymbol{P}_{k+1|k}\boldsymbol{H}_{k+1}^{\mathrm{T}} + \boldsymbol{R}_{k+1}\right)^{-1} \tag{37}$$

The previous EKF formulation is called the discrete EKF, however, in this work a continuous-discrete formulation of the EKF is desired. Consider the continuous state-space given by Eq. (8). The respective Taylor series approximation about $\hat{\boldsymbol{x}}_{k|k}$ and its state covariance matrix are given by Gelb (1974)

$$\dot{\hat{\boldsymbol{x}}}(t) = \boldsymbol{f}\left(\hat{\boldsymbol{x}}(t), \boldsymbol{u}(t)\right) \tag{38}$$

$$\dot{\boldsymbol{P}}(t) = \boldsymbol{F}(t)\boldsymbol{P}(t) + \boldsymbol{P}(t)\boldsymbol{F}(t)^{\mathrm{T}} + \boldsymbol{Q}(t) \tag{39}$$

where from Eq. (9) we obtain

$$\boldsymbol{F}(t) = \left[\frac{\partial}{\partial \boldsymbol{x}}\boldsymbol{f}\left(\boldsymbol{x}, \boldsymbol{u}(t)\right)\right]_{\boldsymbol{x}=\hat{\boldsymbol{x}}_{k|k}} = \begin{bmatrix} \mathbf{0}_{3\times3} & \boldsymbol{I}_3 & \mathbf{0}_{3\times1} & \mathbf{0}_{3\times1} & \mathbf{0}_{3\times3} \\ \mathbf{0}_{3\times3} & \mathbf{0}_{3\times3} & \boldsymbol{B} & \mathbf{0}_{3\times1} & -\left(\boldsymbol{D}^{P/G}\left(\psi\right)\right)^{\mathrm{T}} \\ \mathbf{0}_{1\times3} & \mathbf{0}_{1\times3} & 0 & -1 & \mathbf{0}_{1\times3} \\ \mathbf{0}_{4\times3} & \mathbf{0}_{4\times3} & \mathbf{0}_{4\times1} & \mathbf{0}_{4\times1} & \mathbf{0}_{4\times3} \end{bmatrix}_{\boldsymbol{x}=\hat{\boldsymbol{x}}_{k|k}} \tag{40}$$

with

$$\boldsymbol{B} = \begin{bmatrix} -C\psi\left(\check{a}_{P,y} - \beta_{a,y}\right) - S\psi\left(\check{a}_{P,x} - \beta_{a,x}\right) \\ C\psi\left(\check{a}_{P,x} - \beta_{a,x}\right) - S\psi\left(\check{a}_{P,y} - \beta_{a,y}\right) \\ 0 \end{bmatrix}$$

Similarly, for a i-th landmark it is possible to compute $\boldsymbol{H}_{k+1}^{(i)}$ from Eq. (31) using Eq. (19)-(21)

$$\boldsymbol{H}_{k+1}^{(i)} = \left[\frac{\partial}{\partial \boldsymbol{x}}\boldsymbol{h}^{(i)}\left(\boldsymbol{x}_k\right)\right]_{\boldsymbol{x}=\hat{\boldsymbol{x}}_{k+1|k}} = \begin{bmatrix} -\left(\boldsymbol{D}^{C/G}\left(\psi\right)\right)^{\mathrm{T}} & \mathbf{0}_{3\times3} & \boldsymbol{C} & \mathbf{0}_{3\times4} \end{bmatrix}_{\boldsymbol{x}=\hat{\boldsymbol{x}}_{k|k}} \tag{41}$$

with

$$\boldsymbol{C} = \begin{bmatrix} -C\psi\left(l_x^{(i)} - r_{G,x}^{C/G}\right) - S\psi\left(l_y^{(i)} - r_{G,y}^{C/G}\right) \\ C\psi\left(l_y^{(i)} - r_{G,y}^{C/G}\right) - S\psi\left(l_x^{(i)} - r_{G,x}^{C/G}\right) \\ 0 \end{bmatrix}$$

The complete measurement Jacobian matrix is thus given by

$$\boldsymbol{H}_{k+1} = \begin{bmatrix} \boldsymbol{H}_{k+1}^{(1)} \\ \boldsymbol{H}_{k+1}^{(2)} \\ \vdots \\ \boldsymbol{H}_{k+1}^{(q)} \end{bmatrix}. \tag{42}$$

It is worth to mention that the complexity of the Extended Kalman Filter algorithm is approximately $O\left(q^3\right)$ (Thrun, 2002), that is, the complexity grows in a cubic fashion proportionally to the number of processed landmarks. Thus, the number of used landmarks in the EKF algorithm is a trade-off between accuracy, as greater values of q leads to a preciser estimation, and computational efficiency, that could, depending on the available Hardware/Software, degrade the capability of estimating the desired variables in real-time.

Finally, the complete Continuous-Discrete EKF algorithm is depicted next in Algorithm 1:

Algorithm 1 Continuous-Discrete Extended Kalman Filter

1: **Initial conditions**: $k = 0, \hat{\boldsymbol{x}}_{0|0} = \overline{\boldsymbol{x}}, \mathbf{P}_{0|0} = \overline{\mathbf{P}}$
2: **loop**
3: Prediction:
4: $\hat{\boldsymbol{x}}_{k+1|k} = \text{integrate}\left(\mathbf{f}\left(\hat{x}(t), \boldsymbol{u}(t)\right)\right)$ from t_k to t_{k+1}, with initial conditions $\hat{\boldsymbol{x}}_{0|0}$
5: $\boldsymbol{P}_{k+1|k} = \text{integrate}\left(\mathbf{F}(t)\mathbf{P}(t) + \mathbf{P}(t)\mathbf{F}(t)^{\mathrm{T}} + \mathbf{Q}(t)\right)$ from t_k to t_{k+1}, with initial conditions $\mathbf{P}_{0|0}$
6: Update:
7: $\mathbf{K}_{k+1} = \mathbf{P}_{k+1|k}\mathbf{H}_{k+1}^{\mathrm{T}}\left(\mathbf{H}_{k+1}\mathbf{P}_{k+1|k}\mathbf{H}_{k+1}^{\mathrm{T}} + \boldsymbol{R}_{k+1}\right)^{-1}$
8: $\hat{\boldsymbol{x}}_{k+1|k+1} = \hat{x}_{k+1|k} + \mathbf{K}_{k+1}\left(\boldsymbol{y}_{k+1} - \boldsymbol{h}\left(\hat{\boldsymbol{x}}_{k+1|k}\right)\right)$
9: $\mathbf{P}_{k+1|k+1} = \mathbf{P}_{k+1|k} - \mathbf{K}_{k+1}\mathbf{H}_{k+1}\mathbf{P}_{k+1|k}$
10: $k = k + 1$
11: **end loop**

In this work, the integration is done numerically using a 4th order Runge-Kutta algorithm.

4 COMPUTATIONAL SIMULATION

To evaluate the proposed problem, a simulation platform is used. The simulation environment is composed with a non-linear model of a quadrotor, modeled as in Mahony *et al.* (2012), using a linear Proportional-Derivative (PD) controller, introduced by Dos Santos *et al.* (2013), to follow a predefined trajectory. The model is simulated in a Simulink environment with a Runge-Kutta 4 integration method running at a time step of 0.1 second. The Simulink 3D Animation simulates the environment, containing the visible landmarks, and the UAV navigation. A viewpoint attached to the vehicle simulates the embedded camera and it is fixed to the vehicle translation and rotation about the Z_P axis. The platform stabilization is considered instantaneous and its control dynamics are neglected, as stated in Section 2.

The simulated vehicle has a mass of 1 kg, an inertial matrix of $J = \text{diag}\{0.02, 0.02, 0.03\}$ and the local gravitational acceleration is 9.81 m/s^2. The position controller is a Proportional-Derivative (PD) controller with gains $k_{p,x} = k_{p,y} = k_{p,z} = k_{d,x} = k_{d,y} = k_{d,z} = 4$, where k_p and k_d are the proportional and the derivative gains, respectively. The heading controller is also a PD controller, with gains $k_{p,\psi} = 1.1$ and $k_{d,\psi} = 0.5$. The chosen trajectory is divided into a three-dimensional position trajectory with constant velocity $v_w = 0.2$ m/s^2 and a heading trajectory. The position trajectory chosen is composed of seven waypoints as depicted in Table 1. The heading trajectory used in simulation is defined as a sinusoidal wave with frequency of $2\frac{\pi}{10}$ rad/sec and amplitude $\frac{\pi}{6}$ meters.

Table 1: Position trajectory waypoints.

	1	2	3	4	5	6	7
$\boldsymbol{r}_x$	0	0	1	1	0	0	0
$\boldsymbol{r}_y$	0	0	0	1	1	0	0
$\boldsymbol{r}_z$	1.5	2	2	2	2	2	1.5

The simulation environment contains 25 landmarks that are displaced uniformly on a virtual square grid. The side distance of the grid is 0.5 m in both horizontal and vertical direction. Each landmark has its own unique color that is used in a simple processing algorithm in order to track the landmark's position. The simulated camera has a diagonal field-of-view (FOV) of 0.7854 radian and a focal length $f = 1$ m. Furthermore, the output image has a pixel resolution of 200×300.

As stated in Section 2.1, the state noise vector is defined as a random distribution $\boldsymbol{w} \sim \mathcal{N}(\mathbf{0}_{11\times1}, \boldsymbol{Q})$, where $\boldsymbol{Q} = \text{diag}\left\{\boldsymbol{\sigma}_r^2, \boldsymbol{\sigma}_v^2, \sigma_\psi^2, \sigma_g^2, \boldsymbol{\sigma}_a^2\right\}$ is the covariance matrix formed with the individual variances of $\boldsymbol{w}$. The chosen variances are: $\boldsymbol{\sigma}_r^2 = 1e^{-8}\mathbf{1}_{3\times1}$ m^2, $\boldsymbol{\sigma}_v^2 = 1e^{-8}\mathbf{1}_{3\times1}$ (m/s)^2, $\sigma_\psi^2 = 1e^{-6}$ rad^2, $\sigma_g^2 = 1e^{-8}$ (rad/s)^2 and $\boldsymbol{\sigma}_a^2 = 1e^{-6}$ (m/s^2)^2. Likewise, for the measurement noise vector of the i-th landmark $\boldsymbol{v}_k^{(i)} \sim \mathcal{N}\left(\mathbf{0}_{3\times1}, \boldsymbol{R}_k^{(i)}\right)$, with $\boldsymbol{R}_k^{(i)} = 0.01^2\boldsymbol{I}_3$ m^2. In addition, to test the robustness of the filter, it is introduced an additive zero-mean Gaussian noise in the measurements of the ultrasonic range sensor with variance of $\sigma_u^2 = 0.001^2$ m^2, as well as in the measurements of the camera $\breve{x}_{I_k}^{(i)}$ and $\breve{y}_{I_k}^{(i)}$, with variances of $\sigma_{I,x}^2 = \sigma_{I,y}^2 = 0.01^2$ m^2, simulating the image processing algorithm errors.

The state's initial conditions are also a random sequence $\boldsymbol{x}_0 \sim \mathcal{N}\left(\overline{\boldsymbol{x}}, \overline{\boldsymbol{P}}\right)$, with $\overline{\boldsymbol{x}} = \begin{bmatrix}0 & 0 & 1.5 & \mathbf{0}_{1\times8}\end{bmatrix}^{\mathrm{T}}$ and $\overline{\boldsymbol{P}} = \text{diag}\left\{\boldsymbol{\sigma}_{0,r}^2, \boldsymbol{\sigma}_{0,v}^2, \sigma_{0,\psi}^2, \sigma_{0,g}^2, \boldsymbol{\sigma}_{0,a}^2\right\}$, where $\boldsymbol{\sigma}_{0,r}^2 = \begin{bmatrix}1 & 1 & 0.1^2\end{bmatrix}^{\mathrm{T}}$ m^2, $\boldsymbol{\sigma}_{0,v}^2 = 1e^{-4}\mathbf{1}_{3\times1}$ (m/s)^2, $\sigma_{0,\psi}^2 = \left(\frac{\pi}{4}\right)^2$ rad^2, $\sigma_{0,g}^2 = 1e^{-8}$ (rad/s)^2 and $\boldsymbol{\sigma}_a^2 = 1e^{-6}\mathbf{1}_{3\times1}$ (m/s^2)^2.

4.1 Results

The EKF filter is evaluated via extensive Monte Carlo (MC) simulations. In this work 100 simulation runs are performed for each realization, completing 4 Monte Carlo simulations. For each MC simulation the number of landmarks used in the update phase is changed in order to analyze the behavior of the proposed filter. At the first Monte Carlo simulation, the filter uses a unique landmark. Secondly, the filter uses two of the seen landmarks at a time t_k, taking care of choosing the two most distant landmarks in the image, thus providing better information about the desired states. The third MC simulation uses three landmarks and the fourth uses four. The result is depicted in Table 2.

Table 2: Monte Carlo simulations for different values of landmarks used.

Num. Landmarks (q)	ε_p	σ_p	ε_v	σ_v	ε_ψ	σ_ψ
1	27.4000	26.5498	16.0698	15.5958	42.0808	47.8301
2	13.1834	7.3441	8.8634	6.2686	9.1421	7.5490
3	9.9839	3.6142	8.7425	5.5105	7.6667	4.3710
4	9.3511	3.2089	8.5103	5.1357	7.3083	4.0336

The following figure of merit are used to evaluate the position estimation error:

$$\varepsilon_p \triangleq \frac{1}{N}\sum_{i=1}^{N}\sum_{k=1}^{k_f} e_p^{(i)}(k) \tag{43}$$

$$\sigma_p \triangleq \sqrt{\frac{1}{N}\sum_{i=1}^{N}\left(\sum_{k=1}^{k_f} e_p^{(i)}(k) - \varepsilon_p\right)^2} \tag{44}$$

with

$$e_p^{(i)}(k) \triangleq \| \boldsymbol{r}(k) - \hat{\boldsymbol{r}}(k) \|_2^{(i)}, \quad k = 1, 2, ..., k_f, \tag{45}$$

where the pair $(\varepsilon_p, \sigma_p^2)$ represents the sampling mean and variance of the MC simulation. The $\| \ . \ \|_2^{(i)}$ represents the Euclidean norm of the i-th realization, $\hat{\boldsymbol{r}}(k)$ represents the estimate of the position $\boldsymbol{r} \triangleq \boldsymbol{r}_G^{G/P}$ at the instant k, and N represents the number of simulation realizations. In this case, $N = 100$. Similarly, the velocity $(\varepsilon_v, \sigma_v)$ and heading $(\varepsilon_\psi, \sigma_\psi)$ estimation error are obtained using the same figure of merit, replacing $\boldsymbol{r}$ with $\boldsymbol{v}$ and ψ, respectively. The constant k_f represents the number of samples taken from each realization realization.

From Table 2 it is possible to notice the relationship between the number of landmarks used in the EKF and its accuracy. The more landmarks we use in the update phase of the filter, the preciser is the filter. Nonetheless, as stated in the end of Section 3.2, it comes with a higher computational effort. As can be noted, using only 1 landmark it is not possible to estimate the desired states. In fact, it was expected, since we need at least 2 vector measurements to estimate an unique position and heading estimate (Sun and Crassidis, 2002). Further, considering the other rows of Table 2, it can be seen that there is a significant increase in accuracy from 2 to 3 landmarks, but only a slight increase when 4 landmarks are used. For this reason, we found that using 3 landmarks in the EKF is sufficient to obtain a precise estimation solution to the proposed problem, since greater values of q shows lower tendency to increase the filter's accuracy.

The Figure 4 shows the temporal response of the position, velocity and heading estimation error for the Monte Carlo simulations using 3 landmarks. As can be observed, the filter has higher errors between 0 and 2 seconds of simulation. This occurs mostly due to the large initial conditions errors in position and heading. These position initial conditions also explains the error spike in Figure 4b at approximately 1 second, where the vehicle must abruptly return to follow the position trajectory given by Table 1, increasing its speed. Moreover, it can can be seen that the filter converges in approximately 2 seconds.

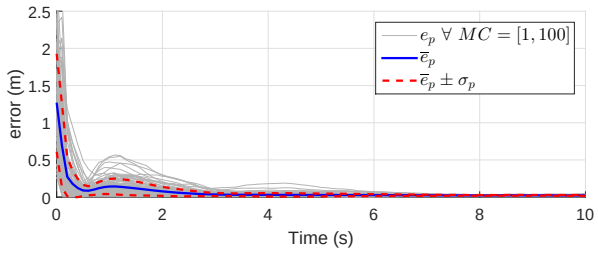

(a) Position Estimation error.

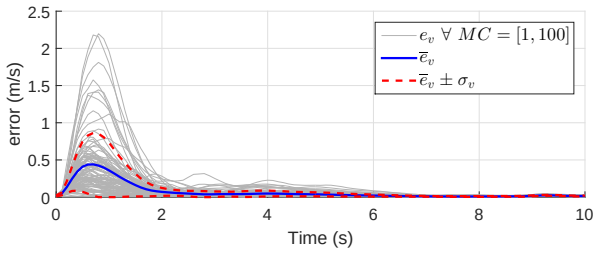

(b) Velocity Estimation error.

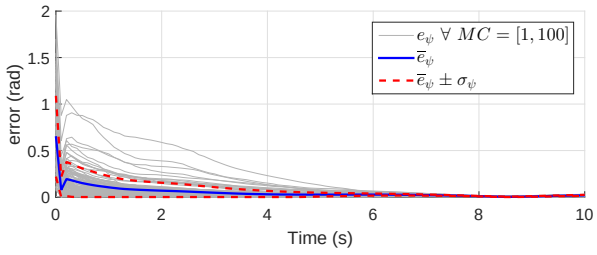

(c) Heading Estimation Error

Figure 4: Monte Carlo simulations using $q = 3$ landmarks.

5 CONCLUSION

The present paper has proposed a method of accurately and robustly estimating the position, velocity and heading of an Unmanned Aerial Vehicle in GNSS-denied environment using an embedded camera, inertial sensors and an aid of an ultrasonic range finder. The method is based on an Extended Kalman Filter that is responsible for the sensor fusion between the different type of sensors and the camera, that capture visible landmarks, whose positions are previously known. The proposed solution was evaluated via computation simulations using a quadrotor vehicle model, but can be

expanded to any UAV with a stabilizing gimbal platform. Moreover, a Monte Carlo simulation with 100 realizations was made to verify the relationship between the filter accuracy and the number of landmarks used. As expected, as higher number of landmarks is used, preciser the filter becomes, but with a higher computational cost. With these results, it could be shown that the filter could successfully estimate the desired states with the given set of sensors. In summary, the proposed estimation method represents a precise and low-cost alternative to the proposed problem. For future work, other filters are being developed to tackle this problem and it will be possible to carry out a comparison of using different approaches to tackle the proposed problem.

6 REFERENCES

Anderson, B.D.O., Moore, J.B. and Eslami, M., 1982. "Optimal Filtering". *IEEE Transactions on Systems, Man, and Cybernetics*, Vol. 12, No. 2, pp. 235–236.

Arulampalam, M., Maskell, S., Gordon, N. and Clapp, T., 2001. "A tutorial on Particle Filters for On-line Non-Linear/Non-Gausssian Bayesin Tracking". *Ieee*, Vol. 50, No. 2, pp. 174–188.

Bay, H., Tuytelaars, T. and Van Gool, L., 2006. "SURF: Speeded Up Robust Features". In *Lecture Notes in Computer Science (including subseries Lecture Notes in Artificial Intelligence and Lecture Notes in Bioinformatics)*, Vol. 3951 LNCS, pp. 404–417.

Beard, R.W., McLain, T.W., Nelson, D.B., Kingston, D. and Johanson, D., 2006. "Decentralized cooperative aerial surveillance using fixed-wing miniature UAVs". *Proceedings of the IEEE*, Vol. 94, No. 7, pp. 1306–1323.

Dos Santos, D.A., Saotome, O. and Cela, A., 2013. "Trajectory control of multirotor helicopters with thrust vector constraints". *2013 21st Mediterranean Conference on Control and Automation, MED 2013 - Conference Proceedings*, pp. 375–379.

Erdos, D., Erdos, A. and Watkins, S.E., 2013. "An experimental UAV system for search and rescue challenge". *IEEE Aerospace and Electronic Systems Magazine*, Vol. 28, pp. 32–37.

Evensen, G., 2003. "The Ensemble Kalman Filter: Theoretical formulation and practical implementation". *Ocean Dynamics*, Vol. 53, No. 4, pp. 343–367.

García Carrillo, L.R., Dzul López, A.E., Lozano, R. and Pégard, C., 2012. "Combining stereo vision and inertial navigation system for a quad-rotor UAV". *Journal of Intelligent and Robotic Systems: Theory and Applications*, Vol. 65, No. 1-4, pp. 373–387.

Gelb, A., 1974. *Applied Optimal Estimation*, Vol. 64.

Gini, G.C. and Marchi, A., 2002. "Indoor Robot Navigation With Single Camera Vision". *Pris*, pp. 67–76.

Hartley, R. and Zisserman, A., 2015. *Multiple view geometry in computer vision*, Vol. 1.

Hoffmann, G.M., Waslander, S.L. and Tomlin, C.J., 2008. "Quadrotor Helicopter Trajectory Tracking Control". *Electrical Engineering*, Vol. 44, No. August, pp. 1–14. URL `http://hoffmann.stanford.edu/papers/GNC08_QuadTraj.pdf`.

Kalman, R.E., 1960. "A New Approach to Linear Filtering and Prediction Problems".

Lowe, D.G., 1999. "Object recognition from local scale-invariant features". *Proceedings of the Seventh IEEE International Conference on Computer Vision*, Vol. 2, No. [8, pp. 1150–1157.

Mahony, R., Kumar, V. and Corke, P., 2012. "Multirotor Aerial Vehicles: Modeling, Estimation, and Control of Quadrotor". *IEEE Robotics & Automation Magazine*, Vol. 19, No. 3, pp. 20–32.

MathWorks, I., 2016. "Simulink 3D Animation User's Guide". URL `http://www.mathworks.com/help/pdf_doc/sl3d/sl3d.pdf`.

Ponce, J. and Forsyth, D., 2012. *Computer vision: a modern approach*.

Primicerio, J., Di Gennaro, S.F., Fiorillo, E., Genesio, L., Lugato, E., Matese, A. and Vaccari, F.P., 2012. "A flexible unmanned aerial vehicle for precision agriculture". *Precision Agriculture*, Vol. 13, No. 4, pp. 517–523.

Shuster, M.D., 1993. "A Survey of Attitude Representations".

Sun, D. and Crassidis, J.L., 2002. "Observability Analysis of Six-Degree-of-Freedom Configuration Determination Using Vector Observations". *Jgcd*, Vol. 25, No. 6, pp. 1149–1157.

Thrun, S., 2002. "Probabilistic robotics". *Communications of the ACM*, Vol. 45, No. 3, pp. 1999–2000.

Trawny, N., Mourikis, A.I., Roumeliotis, S.I., Johnson, A.E. and Montgomery, J.F., 2007. "Vision-aided inertial navigation for pin-point landing using observations of mapped landmarks". *Journal of Field Robotics*, Vol. 24, No. 5, pp. 357–378.

Wendel, J., Meister, O., Schlaile, C. and Trommer, G.F., 2006. "An integrated GPS/MEMS-IMU navigation system for an autonomous helicopter". *Aerospace Science and Technology*, Vol. 10, No. 6, pp. 527–533.

Zhang, L., Li, T., Yang, H., Zhang, S., Cai, H. and Qian, S., 2015. "Unscented Kalman Filtering for Relative Spacecraft Attitude and Position Estimation". *Journal of Navigation*, Vol. 68, pp. 528–548.